Learnable Transform-Assisted Tensor Decomposition for Spatio-Irregular Multidimensional Data Recovery

HAO ZHANG, TING-ZHU HUANG, and XI-LE ZHAO, School of Mathematical Sciences, University of Electronic Science and Technology of China, Chengdu, China
SHUQIN ZHANG, School of Mathematical Sciences, Fudan University, Shanghai, China
JIN-YU XIE, School of Mathematical Sciences, University of Electronic Science and Technology of China, Chengdu, China
TAI-XIANG JIANG, School of Computing and Artificial Intelligence, Southwestern University of Finance and Economics, Chengdu, China
MICHAEL K. NG, Department of Mathematics, Hong Kong Baptist University, Hong Kong, Hong Kong

Tensor decompositions have been successfully applied to multidimensional data recovery. However, classical tensor decompositions are not suitable for emerging spatio-irregular multidimensional data (i.e., spatio-irregular tensor), whose spatial domain is non-rectangular, e.g., spatial transcriptomics data from bioinformatics and semantic units from computer vision. By using preprocessing (e.g., zero-padding or element-wise 0-1 weighting), the spatio-irregular tensor can be converted to a spatio-regular tensor and then classical tensor decompositions can be applied, but this strategy inevitably introduces bias information, leading to artifacts. How to design a tensor-based method suitable for emerging spatio-irregular tensors is an imperative challenge. To address this challenge, we propose a learnable transform-assisted tensor singular value decomposition (LTA-TSVD) for spatio-irregular tensor recovery, which allows us to leverage the intrinsic structure behind the spatio-irregular tensor. Specifically, we design a learnable transform to project the original spatio-irregular tensor into its latent spatio-regular tensor, and then the latent low-rank structure is captured by classical TSVD on the resulting regular tensor. Empowered by LTA-TSVD, we develop spatio-irregular low-rank tensor completion (SIR-LRTC) and spatio-irregular tensor robust principal component analysis (SIR-TRPCA) models for the spatio-irregular tensor imputation and denoising respectively, and we design corresponding solving algorithms with theoretical convergence. Extensive experiments including the spatial transcriptomics data imputation and hyperspectral image denoising show SIR-LRTC and SIR-TRPCA are superior performance to competing approaches and benefit downstream applications.

1 Introduction

With the development of information technology, real-world data is usually more than two dimensions [6, 8, 28, 39]. However, multidimensional data often suffers from corruption (e.g., elements missing and noise) in acquisition and transmission [7, 20, 38], which hinders the subsequent application, such as object recognition [23], classification [44, 45], and segmentation [50]. Thus, recovering multidimensional data enhances the quality of the observed data and enables the recovered results to help subsequent applications [43, 53].

Real-world multidimensional data can be mathematically represented by a tensor [11, 16, 17, 33, 35]. In this article, we focus on three-way tensors. The standard three-way tensor can be considered to consist of several rectangular frontal slices of the same size, i.e., the standard three-way tensor is a spatio-regular tensor. For instance, Figure 1 provides two real-world examples of the spatio-regular tensor. Due to the powerful representation ability, tensor-based methods have recently received increasing attention in the field of multidimensional data recovery.

The principal idea behind tensor-based multidimensional data recovery is to exploit the low-rankness of the multidimensional data. Two classical low-rank tensor-based models are **low-rank tensor completion (LRTC)** and **tensor robust principal component analysis (TRPCA)**, which can be employed for missing elements imputation and sparse noise removal, respectively. Considering the observed three-way tensor $\mathcal{Y} \in \mathbb{R}^{n_1 \times n_2 \times n_3}$, the LRTC and TRPCA models can be mathematically formulated as

$$\min_{\mathcal{X}} \ \text{rank}_t(\mathcal{X}), \ \ \text{s.t.} \ \mathcal{Y}_\Omega = \mathcal{X}_\Omega, \tag{1}$$

and

$$\min_{\mathcal{X}} \ \text{rank}_t(\mathcal{X}), \ \ \text{s.t.} \ \mathcal{Y} = \mathcal{X} + \mathcal{S}, \tag{2}$$

where $\text{rank}_t(\cdot)$ is the low-rank tensor regularizer, $\mathcal{X} \in \mathbb{R}^{n_1 \times n_2 \times n_3}$ is the recovered tensor, the constraint $\mathcal{Y}_\Omega = \mathcal{X}_\Omega$ enforces the entries of $\mathcal{X}$ in index Ω equal to the corresponding entries of the observation $\mathcal{Y}$ in the LRTC model, and $\mathcal{S}$ is the sparse component in the TRPCA model.

How to design the low-rank tensor regularizer of Equations (1) and (2) has a considerable effect on the multidimensional data recovery performance. Different from the matrix rank, definition of tensor rank relies on different tensor decompositions. **CANDECOMP/PARAFAC (CP)** decomposition decomposes a tensor as sum of the rank-one tensors [15]. CP rank is defined as the minimal number of the sum of the rank-one tensors [15]. Unfortunately, directly minimizing CP rank of a tensor is usually NP-hard [14]. Tucker decomposition decomposes a tensor into a core tensor multiplied by matrices along each mode [36], which introduces the multilinear rank. The multilinear rank is a vector, which consists of the ranks of each mode's unfolding matrix [36]. Many multidimensional data recovery methods were also inspired by the multilinear rank minimization like HaLRTC [24]
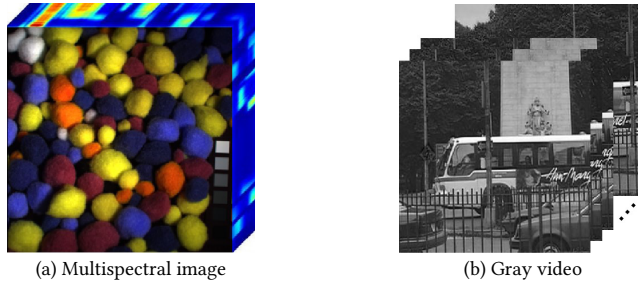
(a) Multispectral image   (b) Gray video

Fig. 1. Real-world examples of the spatio-regular tensor. (a) The multispectral image is a three-way tensor with the rectangular spatial domain, where mode 3-fibers are the same length. (b) The gray video is a three-way tensor with the rectangular spatial domain, where mode 3-fibers are the same length.

and TMac [40]. To tackle the curse of dimensionality of Tucker decomposition, tensor network decompositions were developed, like **tensor train (TT)** decomposition and **tensor ring (TR)** decomposition [4, 9, 10, 32, 51]. TT and TR decompositions are more effective in capturing the low-rank structure of multidimensional data with more than three modes, where the tensor is decomposed into several factors like three-way tensors or matrices. Bengua et al. [4] proposed two surrogates of TT rank for color video recovery. Yu et al. [42] considered the TR nuclear norm for visual data imputation. Additionally, Zheng et al. [52] exploited the connection of each factor of the tensor network decomposition and developed the fully connected tensor network decomposition for LRTC.

Attributed to beautiful algebraic properties, the **tensor singular value decomposition (TSVD)** has received increasing attention in three-way tensor recovery. TSVD introduces the tubal rank [19, 21, 37, 47], which is defined as the number of non-zero mode-3 fibers of the f-diagonal tensor from the TSVD operator. As a convex surrogate of the tubal rank, **tensor nuclear norm (TNN)** has successfully been applied to multidimensional data recovery. Zhang et al. [49] and Lu et al. [26] proposed TNN-based LRTC and TRPCA models, respectively. Different from other tensor decomposition-based regularizers, TNN can be seen as a transform-based low-rank regularizer because TNN exploits the low-rankness of the frontal slice of the tensor under a predefined **discrete Fourier transform (DFT)** along the third mode [21]. Lu et al. [27] and Jiang et al. [18] introduced the **discrete Cosine transform (DCT)** and framelet transform into the TSVD framework for LRTC, respectively.

Moreover, PARAFAC2 decomposition [13] is developed for the three-way tensor, whose frontal slices are rectangles of different sizes, e.g., amino acid data [12] and electronic health records [1]. In summary, these classical tensor decompositions are suitable for the spatio-regular tensor, whose spatial domain is rectangular.

Spatio-Irregular Multidimensional Data: Due to technological advancements, spatio-irregular multidimensional data (i.e., spatio-irregular tensor) has been emerging, such as spatial transcriptomics data from bioinformatics and semantic units from computer vision. The spatio-irregular tensor is a tensor with the non-rectangular spatial domain, where mode 3-fibers are the same length. Figure 2 shows two real-world spatio-irregular tensors: (a) Spatial transcriptomics data of the organ is a typical spatio-irregular tensor, whose spatial domain is defined by the shape of the organ slice [2]; (b) Semantic units from superpixels segmentation algorithm are spatio-irregular tensors, where each semantic unit (i.e., superpixel) is a tensor with the non-rectangular spatial domain [46]. However, previous tensor-based methods were mainly developed for classical spatio-regular tensors, which cannot be directly applied to spatio-irregular tensors (see sub-figure (c) of Figure 3 as an example).

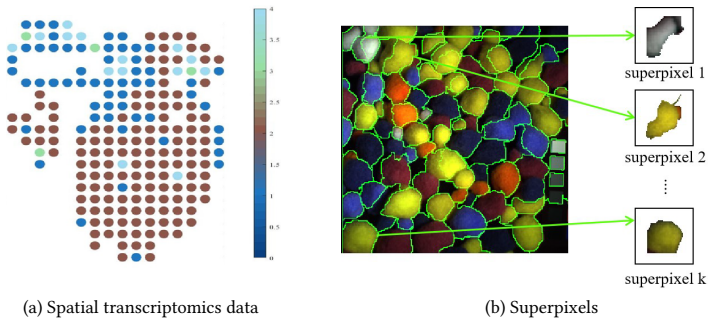(a) Spatial transcriptomics data   (b) Superpixels

Fig. 2. Real-world examples of spatio-irregular tensors. (a) The spatial transcriptomics data of the human heart visualized in 2D. (b) Semantic units (i.e., superpixels) from superpixels segmentation algorithm on MSI *Pompoms*.

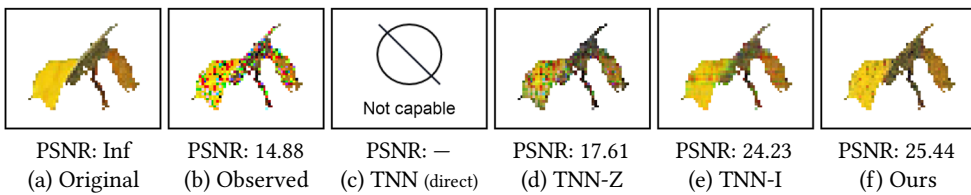| PSNR: Inf | PSNR: 14.88 | PSNR: — | PSNR: 17.61 | PSNR: 24.23 | PSNR: 25.44 |
| (a) Original | (b) Observed | (c) TNN (direct) | (d) TNN-Z | (e) TNN-I | (f) Ours |

Fig. 3. An experimental example of superpixel denoising. This superpixel is from the color image *Butterfly* and corrupted by salt and pepper noise with the ratio = 0.3. Here, TNN cannot be directly applied to the original spatio-irregular tensor (see sub-figure (c)). By using zero-padding or interpolation, TNN can be applied to the resulting spatio-regular tensor (see sub-figures (d) and (e)). Our method is suitable for the spatio-irregular tensor while TNN-Z and TNN-I introduce artifacts (see sub-figures (d), (e), and (f)).

By using preprocessing (e.g., zero-padding [12] or interpolation [41]), we can convert the spatio-irregular tensor to a regular tensor and then apply classical tensor-based methods (e.g., TNN). However, this strategy inevitably introduces bias information, leading to artifacts (see sub-figures (d) and (e) of Figure 3). In summary, classical tensor-based methods are not suitable for spatio-irregular tensors, hindering the spatio-irregular tensor processing and analysis. How to design a tensor-based method suitable for emerging spatio-irregular tensors is an imperative challenge.

To address this challenge, we develop a fundamental tensor decomposition for emerging spatio-irregular tensors. Specifically, the spatio-irregular tensor can be lifted to a latent regular tensor, which usually exhibits a low-rank structure. From Figure 4, we can observe that the singular values' energy of the latent regular tensor is significantly concentrated, which indicates the latent regular tensor exhibits significant low-rankness. Motivated by this observation, we propose a **learnable transform-assisted tensor singular value decomposition (LTA-TSVD)** for spatio-irregular tensor recovery. Figure 5 provides the flowchart of the proposed method. In LTA-TSVD, we design a learnable transform to project the original spatio-irregular tensor into its latent spatio-regular tensor, and then the latent low-rank structure is captured by classical TSVD on the resulting regular tensor. In this process, the proposed method uses the learnable spatial transform to project the original spatio-irregular tensor into a latent regular tensor while preserving the essential low-rankness of the spatio-irregular tensor without introducing extra bias information. We further compare the low-rankness of the spatio-irregular tensor with preprocessing (e.g., zero-padding and
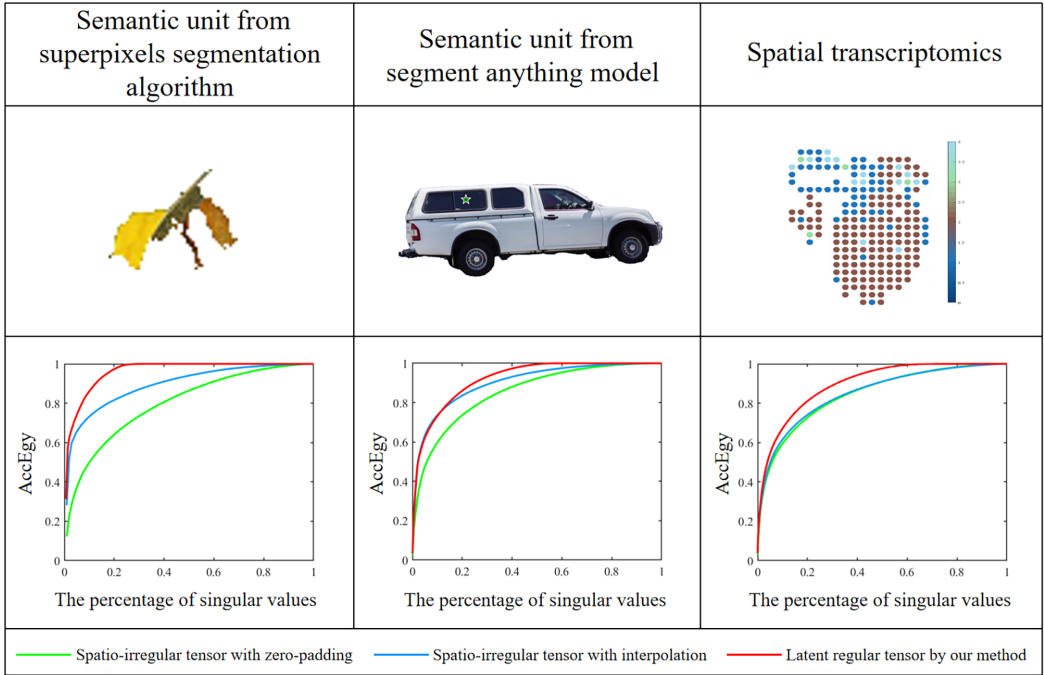
Fig. 4. The accumulation energy ratio of singular values (AccEgy) curves of the spatio-irregular tensor with zero-padding, the spatio-irregular tensor with interpolation, and the latent regular tensor by our method for diverse spatio-irregular multidimensional data. Here, AccEgy $= (\sum_{k=1}^{n_3} \sum_{i=1}^{r} \sigma_i^k)/(\sum_{k=1}^{n_3} \sum_{i}^{r_{\max}} \sigma_i^k)$, where σ_i^k is the ith singular value of the kth frontal slice under the TSVD framework, r is the first r singular values of the kth slice, and $r_{\max}$ is the total numbers of singular values of the kth slice.
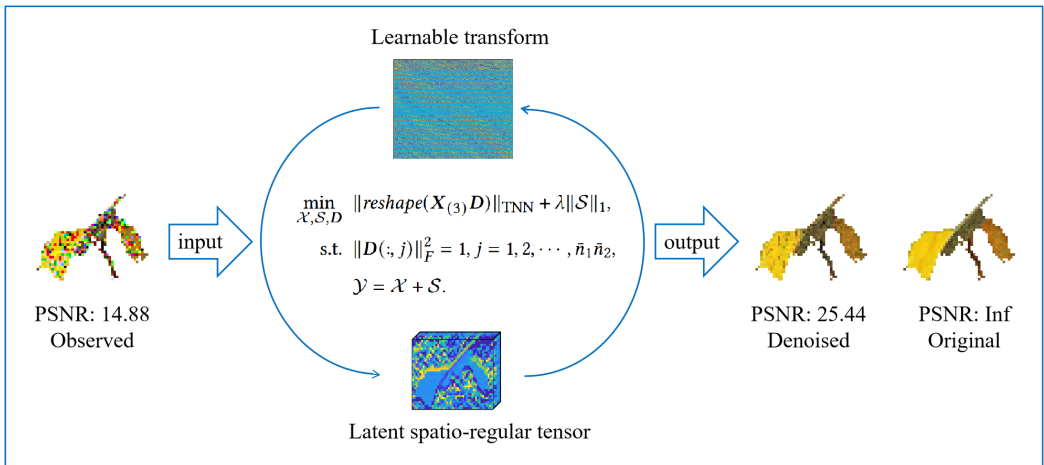
Fig. 5. The flowchart of the proposed method. This is an example of superpixel denoising. Here, $\mathcal{Y}$ is the observed spatio-irregular tensor with n_3 frontal slices and l mode-3 fibers, $\mathcal{X}$ is the denoised tensor, $X_{(3)} \in \mathbb{R}^{n_3 \times l}$ is the mode-3 matricization of $\mathcal{X}$, $D \in \mathbb{R}^{l \times \bar{n}_1 \bar{n}_2}$ is the learnable transform, *reshape* re-arrays $(X_{(3)}D)$ as the latent spatio-regular tensor of size $\bar{n}_1 \times \bar{n}_2 \times n_3$, $\mathcal{S}$ is the sparse noise, $\| \cdot \|_1$ is l_1 norm, $\| \cdot \|_F$ is Frobenius norm, $\| \cdot \|_{\text{TNN}}$ is tensor nuclear norm, and λ is the parameter to balance regularizers.

Table 1.   Basic Definitions

Notations	Explanation
$x, \boldsymbol{x}, \boldsymbol{X}, \mathcal{X}$	scalar, vector, matrix, tensor
$\mathcal{X}_{ijk}, \mathcal{X}(i, j, k)$	the $\{i, j, k\}$-th element of the three-way tensor $\mathcal{X}$
$\mathcal{X}(:, :, k), \mathcal{X}^{(k)}$	the k-th frontal slice of the three-way tensor $\mathcal{X}$
$\boldsymbol{X}(:, j)$	the j-th column of the matrix $\boldsymbol{X}$
$\|\mathcal{X}\|_F$	Frobenius norm: $\|\mathcal{X}\|_F = \sqrt{\sum_i \sum_j \sum_k \mathcal{X}_{ijk}^2}$
$\|\mathcal{X}\|_1$	l_1 norm: $\|\mathcal{X}\|_1 = \sum_i \sum_j \sum_k |\mathcal{X}_{ijk}|$
$\sigma_j(\boldsymbol{X})$	the j-th singular value of $\boldsymbol{X}$
$\boldsymbol{X}_{(k)}$	mode-k matricization of $\mathcal{X}$
$vec(\boldsymbol{X})$	vectorization of $\boldsymbol{X}$
$\boldsymbol{X}^\top$	transpose of $\boldsymbol{X}$
$\boldsymbol{X}^{-1}$	inverse of $\boldsymbol{X}$
$\boldsymbol{I}_n$	identity matrix with size $n \times n$

interpolation) and the latent regular tensor by our method in Figure 4. We can observe that the singular values' energy of the latent regular tensor by our method is significantly more concentrated than that of the spatio-irregular tensor with preprocessing, which indicates our method can better exploit the essential low-rankness of the spatio-irregular tensor as compared with traditional tensor-based methods with preprocessing. The experimental results in Figure 3 also show that the traditional tensor-based method with the preprocessing (e.g., TNN with zero-padding and interpolation) inevitably introduces bias information, leading to significant artifacts (see sub-figures (d) and (e) of Figure 3). Compared with the traditional tensor-based method with the preprocessing, our method better exploits the essential low-rankness without introducing extra bias information, thus avoiding artifacts (see sub-figure (f) of Figure 3).

Our contributions are summarized as the following two folds:

(a) We propose an LTA-TSVD for spatio-irregular multidimensional data recovery, which allows us to leverage the intrinsic structure behind the spatio-irregular multidimensional data. Empowered by LTA-TSVD, we develop corresponding **spatio-irregular low-rank tensor completion (SIR-LRTC)** and **spatio-irregular tensor robust principal component analysis (SIR-TRPCA)** models for spatio-irregular multidimensional data imputation and denoising.

(b) We elaborately design **proximal alternating minimization (PAM)**-based algorithms for solving the resulting models and establish the theoretical convergence. Extensive experiments including the spatial transcriptomics data imputation and **hyperspectral image (HSI)** denoising show the proposed method is superior performance to competing approaches and benefits downstream applications.

2   Preliminaries

Some common symbols used in this article are provided in Table 1. In this article, we mainly consider the three-way tensor.

2.1 TSVD and TNN

Here, we introduce the TSVD briefly, which is a classical tensor decomposition to exploit the low-rank structure of the spatio-regular three-way tensor. For $\mathcal{X} \in \mathbb{R}^{n_1 \times n_2 \times n_3}$, its mode-3 matricization $X_{(3)} \in \mathbb{R}^{n_3 \times n_1 n_2}$ can be calculated by the mode-3 unfolding operator, i.e.,

$$X_{(3)} = unfold_3(\mathcal{X}) = \left(vec(\mathcal{X}(:, :, 1)), vec(\mathcal{X}(:, :, 2)), \dots, vec(\mathcal{X}(:, :, n_3))\right)^\top, \quad (3)$$

and the inverse operator of mode-3 unfolding is defined as $fold_3(unfold_3(\mathcal{X})) = \mathcal{X}$.

Then, the mode-3 tensor-matrix product $\times_3$ can be defined as $\mathcal{X} \times_3 Y = fold_3(Y X_{(3)})$. $\bar{\mathcal{X}}$ is defined as the tensor generated by DFT on each mode-3 fiber of $\mathcal{X}$, i.e., $\bar{\mathcal{X}} = \mathcal{X} \times_3 F$, where F is the DFT matrix. $\mathcal{X}$ can also be computed via the inverse DFT, i.e., $\mathcal{X} = \bar{\mathcal{X}} \times_3 F^{-1}$. In particular, the transpose of a tensor $\mathcal{X} \in \mathbb{R}^{n_1 \times n_2 \times n_3}$ is defined as $\mathcal{X}^\top \in \mathbb{R}^{n_2 \times n_1 \times n_3}$ by transposing each of the frontal slices and then reversing the order of transposed frontal slices 2 through n_3 [21]. $\mathcal{I} \in \mathbb{R}^{n \times n \times n_3}$ is the identity tensor, whose first frontal slice is the $n \times n$ identity matrix and other frontal slices are all zeros [21].

Definition 2.1 (Facewise Product [21]). The facewise product of $\mathcal{X} \in \mathbb{R}^{n_1 \times l \times n_3}$ and $\mathcal{Y} \in \mathbb{R}^{l \times n_2 \times n_3}$ is $\mathcal{Z} = \mathcal{X} \triangle \mathcal{Y}$, where $\mathcal{Z}(:, :, k) = \mathcal{X}(:, :, k)\mathcal{Y}(:, :, k)$.

Definition 2.2 (Tensor-Tensor Product [21]). The tensor-tensor product (t-product) of $\mathcal{X} \in \mathbb{R}^{n_1 \times l \times n_3}$ and $\mathcal{Y} \in \mathbb{R}^{l \times n_2 \times n_3}$ is $\mathcal{Z} = \mathcal{X} * \mathcal{Y} =$ and $\mathcal{Z}$ of size $n_1 \times n_2 \times n_3$, where

$$\mathcal{Z} = \mathcal{X} * \mathcal{Y} = ((\mathcal{X} \times_3 F) \triangle (\mathcal{Y} \times_3 F)) \times_3 F^{-1}. \quad (4)$$

Definition 2.3 (Orthogonal Tensor [21]). If $\mathcal{O} \in \mathbb{R}^{n_1 \times n_2 \times n_3}$ satisfies $\mathcal{O}^\top * \mathcal{O} = \mathcal{O} * \mathcal{O}^\top = \mathcal{I}$, it is orthogonal.

Definition 2.4 (TSVD [21]). The TSVD of $\mathcal{X} \in \mathbb{R}^{n_1 \times n_2 \times n_3}$ is formulated as

$$\mathcal{X} = \mathcal{U} * \mathcal{S} * \mathcal{V}^\top, \quad (5)$$

where $\mathcal{S} \in \mathbb{R}^{n_1 \times n_2 \times n_3}$ is a f-diagonal tensor and $\mathcal{U} \in \mathbb{R}^{n_1 \times n_1 \times n_3}$ and $\mathcal{V} \in \mathbb{R}^{n_2 \times n_2 \times n_3}$ are orthogonal tensors.

Definition 2.5 (TNN [21]). For $\mathcal{X} \in \mathbb{R}^{n_1 \times n_2 \times n_3}$, its TNN can be computed via the summation of the nuclear norm of frontal slices from $\bar{\mathcal{X}} = \mathcal{X} \times_3 F$, i.e.,

$$\|\mathcal{X}\|_{\text{TNN}} = \frac{1}{n_3} \sum_{k=1}^{n_3} \|\bar{\mathcal{X}}(:, :, k)\|_* = \frac{1}{n_3} \sum_{k=1}^{n_3} \sum_j \sigma_j(\bar{\mathcal{X}}(:, :, k)) = \sum_j \mathcal{S}(j, j, 1), \quad (6)$$

where $\mathcal{S}$ is the f-diagonal tensor from TSVD of $\mathcal{X}$.

3 Main Results

In this section, we will introduce the proposed LTA-TSVD, the resulting imputation (SIR-LRTC) and denoising (SIR-TRPCA) models, and the corresponding solving algorithm for spatio-irregular tensors.

We first provide basic definitions and operations for spatio-irregular tensors. The spatio-irregular tensor is a tensor with the non-rectangular spatial domain, where mode 3-fibers are the same length (see Figure 2 for real-world examples).

Definition 3.1 (Mode-3 Matricization of Spatio-Irregular Tensor). For a spatio-irregular tensor $\mathcal{X}$ with n_3 frontal slices and l mode-3 fibers, its mode-3 matricization can be defined as unfolding mode-3 fibers of $\mathcal{X}$ as a matrix, i.e.,

$$X_{(3)} = ir\text{-}unfold_3(\mathcal{X}) = \left(\mathcal{X}^{[1]}, \mathcal{X}^{[2]}, \dots, \mathcal{X}^{[l]}\right), \quad (7)$$

where $\mathcal{X}^{[k]}$ is the kth mode-3 fiber of $\mathcal{X}$ ($k = 1, 2, \ldots, l$), $X_{(3)} \in \mathbb{R}^{n_3 \times l}$, and the inverse process of the mode-3 matricization of spatio-irregular tensor $\mathcal{X}$ can be defined as $\mathcal{X} = \textit{ir-fold}_3(X_{(3)})$.

3.1 LTA-TSVD for Spatio-Irregular Tensors

Now, we begin to define LTA-TSVD for spatio-irregular tensors, which allows us to leverage the intrinsic structure behind the spatio-irregular tensor. In LTA-TSVD, we use a learnable transform to project the original spatio-irregular tensor into its latent spatio-regular tensor, and then the latent low-rank structure is captured by classical TSVD on the resulting regular tensor.

We first define the latent spatio-regular tensor with the help of the learnable transform.

Definition 3.2 (*Latent Spatio-Regular Tensor*). For a spatio-irregular tensor $\mathcal{X}$ with n_3 frontal slices and l mode-3 fibers, its latent spatio-regular tensor $\mathcal{L} \in \mathbb{R}^{\bar{n}_1 \times \bar{n}_2 \times n_3}$ is

$$\mathcal{L} = \textit{reshape}(X_{(3)}D), \tag{8}$$

where $D \in \mathbb{R}^{l \times \bar{n}_1 \bar{n}_2}$ is the learnable transform, *reshape* re-arrays $(X_{(3)}D)$ as the spatio-regular tensor of size $\bar{n}_1 \times \bar{n}_2 \times n_3$, $L_{(3)} = X_{(3)}D$, and $\|D(:,j)\|_F^2 = 1$ ($j = 1, 2, \cdots, \bar{n}_1 \bar{n}_2$).

Then, we define LTA-TSVD for spatio-irregular tensors as follows.

Definition 3.3 (*LTA-TSVD*). For a spatio-irregular tensor $\mathcal{X}$ with n_3 frontal slices and l mode-3 fibers, its LTA-TSVD is defined as

$$\mathcal{L} = \mathcal{U}_{\mathcal{L}} * \mathcal{S}_{\mathcal{L}} * \mathcal{V}_{\mathcal{L}}^{\top}, \tag{9}$$

where $\mathcal{L} \in \mathbb{R}^{\bar{n}_1 \times \bar{n}_2 \times n_3}$ is the latent spatio-regular tensor of $\mathcal{X}$, $\mathcal{S}_{\mathcal{L}} \in \mathbb{R}^{\bar{n}_1 \times \bar{n}_2 \times n_3}$ is a f-diagonal tensor, and $\mathcal{U}_{\mathcal{L}} \in \mathbb{R}^{\bar{n}_1 \times \bar{n}_1 \times n_3}$ and $\mathcal{V}_{\mathcal{L}} \in \mathbb{R}^{\bar{n}_2 \times \bar{n}_2 \times n_3}$ are orthogonal tensors.

Based on LTA-TSVD, we can define the **LTA-TSVD-based tensor nuclear norm (LTA-TNN)** to leverage the intrinsic structure behind the spatio-irregular tensor.

Definition 3.4 (*LTA-TNN*). For a spatio-irregular tensor $\mathcal{X}$ with n_3 frontal slices and l mode-3 fibers, its LTA-TNN is

$$\|\mathcal{X}\|_{\text{LTA-TNN}} = \|\textit{reshape}(X_{(3)}D)\|_{\text{TNN}} = \sum_j \mathcal{S}_{\mathcal{L}}(j, j, 1), \tag{10}$$

where $\mathcal{S}_{\mathcal{L}}$ is the f-diagonal tensor from LTA-TSVD of the spatio-irregular tensor $\mathcal{X}$.

3.2 The Proposed SIR-LRTC and SIR-TRPCA Models

Empowered by LTA-TSVD and LTA-TNN, we propose SIR-LRTC and SIR-TRPCA models for spatio-irregular tensor imputation and denoising, respectively. Specifically, the imputation model (SIR-LRTC) can be formulated as

$$\begin{aligned}
\min_{\mathcal{X}, D} \quad & \|\textit{reshape}(X_{(3)}D)\|_{\text{TNN}}, \\
\text{s.t.} \quad & \|D(:,j)\|_F^2 = 1, j = 1, 2, \cdots, \bar{n}_1 \bar{n}_2, \\
& \mathcal{Y}_{\Omega} = \mathcal{X}_{\Omega},
\end{aligned} \tag{11}$$

where $\mathcal{Y}$ is the observed spatio-irregular tensor with n_3 frontal slices and l mode-3 fibers, $\mathcal{X}$ is the imputed tensor, $X_{(3)} \in \mathbb{R}^{n_3 \times l}$ is the mode-3 matricization of $\mathcal{X}$, $D \in \mathbb{R}^{l \times \bar{n}_1 \bar{n}_2}$ is the learnable transform, *reshape* re-arrays $(X_{(3)}D)$ as the latent spatio-regular tensor of size $\bar{n}_1 \times \bar{n}_2 \times n_3$, and the constraint $\mathcal{Y}_{\Omega} = \mathcal{X}_{\Omega}$ enforces the entries of $\mathcal{X}$ in index Ω equal to the corresponding entries of the observation $\mathcal{Y}$.

Similarly, the denoising model (SIR-TRPCA) can be formulated as

$$\min_{\mathcal{X},\mathcal{S},D} \|reshape(X_{(3)}D)\|_{\text{TNN}} + \lambda\|\mathcal{S}\|_1,$$
$$\text{s.t. } \|D(:,j)\|_F^2 = 1, j = 1, 2, \cdots, \bar{n}_1\bar{n}_2, \tag{12}$$
$$\mathcal{Y} = \mathcal{X} + \mathcal{S}.$$

where $\mathcal{Y}$ is the observed spatio-irregular tensor with n_3 frontal slices and l mode-3 fibers, $\mathcal{X}$ is the denoised tensor, $X_{(3)} \in \mathbb{R}^{n_3 \times l}$ is the mode-3 matricization of $\mathcal{X}$, $D \in \mathbb{R}^{l \times \bar{n}_1\bar{n}_2}$ is the learnable transform, $reshape$ re-arrays $(X_{(3)}D)$ as the latent spatio-regular tensor of size $\bar{n}_1 \times \bar{n}_2 \times n_3$, $\mathcal{S}$ is the sparse noise, and λ is the parameter to balance regularizers.

3.3 Solving Algorithms for the Proposed Models

Since the proposed models are strongly nonconvex, we elaborately design corresponding solving algorithms based on the PAM framework [3]. We first introduce indicator functions as

$$\delta_{\mathcal{C}}(D) = \begin{cases} 0 & \text{if } D \in \mathcal{C} = \{D : \|D(:,j)\|_F^2 = 1\}, j = 1, 2, \cdots, \bar{n}_1\bar{n}_2, \\ +\infty & \text{otherwise,} \end{cases}$$
$$\delta_{\mathcal{B}}(\mathcal{X}) = \begin{cases} 0 & \text{if } \mathcal{X} \in \mathcal{B} = \{\mathcal{X} : \mathcal{Y}_\Omega = \mathcal{X}_\Omega\}, \\ +\infty & \text{otherwise.} \end{cases} \tag{13}$$

Then, to solve Equations (11) and (12), we introduce auxiliary variable $\mathcal{L} = reshape(X_{(3)}D)$ and reformulate problems (11) and (12) as the following unconstrained optimizations, i.e.,

$$\min_{\mathcal{L},\mathcal{X},D} \|\mathcal{L}\|_{\text{TNN}} + \frac{\gamma}{2}\|\mathcal{L} - reshape(X_{(3)}D)\|_F^2 + \delta_{\mathcal{C}}(D) + \delta_\Omega(\mathcal{X}), \tag{14}$$

and

$$\min_{\mathcal{L},\mathcal{X},\mathcal{S},D} \|\mathcal{L}\|_{\text{TNN}} + \lambda\|\mathcal{S}\|_1 + \frac{\gamma}{2}\|\mathcal{L} - reshape(X_{(3)}D)\|_F^2 + \frac{\mu}{2}\|\mathcal{Y} - \mathcal{X} - \mathcal{S}\|_F^2 + \delta_{\mathcal{C}}(D), \tag{15}$$

where μ and γ are penalty parameters. When μ and γ are large enough, problems (14) and (15) are equivalent to the original problems (11) and (12).

Then, under the PAM framework, the original problem can be decoupled into simpler subproblems, which are alternatively updated. Specifically, subproblems for updating each variable are as follows.

— Subproblem for updating $\mathcal{L}$: This subproblem is a typical **tensor singular value thresholding (TSVT)** problem [26], i.e.,

$$\mathcal{L}^{t+1} = \arg\min_{\mathcal{L}} \|\mathcal{L}\|_{\text{TNN}} + \frac{\gamma}{2}\|\mathcal{L} - reshape(X_{(3)}^t D^t)\|_F^2 + \frac{\rho}{2}\|\mathcal{L} - \mathcal{L}^t\|_F^2,$$
$$= \text{TSVT}\left(\frac{\gamma reshape(X_{(3)}^t D^t) + \rho\mathcal{L}^t}{\gamma + \rho}, \frac{1}{\gamma + \rho}\right), \tag{16}$$

where ρ is the stepsizes parameter of the proximal term. Define $\mathcal{X} = \mathcal{U} * \mathcal{S} * \mathcal{V}^\top$ be the TSVD of $\mathcal{X}$, and then the corresponding TSVT operator is defined as $\text{TSVT}(\mathcal{X}, \tau) = \mathcal{U} * \mathcal{S}_\tau * \mathcal{V}^\top$ $(\tau > 0)$, where $\mathcal{S}_\tau = (\bar{\mathcal{S}} - \tau)_+ \times_3 F^{-1}$ and $(\bar{\mathcal{S}} - \tau)_+ = \max(\bar{\mathcal{S}}_{ijk} - \tau, 0)$ [26].

— Subproblem for updating D: This subproblem is a typical least-square problem with the constraint $\|D(:,j)\|_F^2 = 1$, i.e.,

$$D^{t+1} = \arg\min_{D} \frac{\gamma}{2}\|\mathcal{L}^{t+1} - reshape(X_{(3)}^t D)\|_F^2 + \frac{\rho}{2}\|D - D^t\|_F^2,$$

$$= \arg\min_{D} \frac{\gamma}{2}\|L_{(3)}^{t+1} - X_{(3)}^t D\|_F^2 + \frac{\rho}{2}\|D - D^t\|_F^2, \tag{17}$$

$$= P_{\mathcal{C}}((\gamma X_{(3)}^{\top t} X_{(3)}^t + \rho I)^{-1}(\gamma X_{(3)}^{\top t} L_{(3)}^{t+1} + \rho D^t)),$$

where $P_{\mathcal{C}}$ is a operator satisfying $P_{\mathcal{C}}(G) = G(:, j)/\|G(:, j)\|_F$.

The subproblems for updating $\mathcal{L}$ and D are same for solving SIR-LRTC and SIR-TRPCA. Next, the subproblems for updating $\mathcal{X}$ and $\mathcal{S}$ are as follows.

— Subproblem for updating $\mathcal{X}$ in SIR-LRTC: This subproblem is a typical least-square problem with the constraint $\mathcal{X}_\Omega = \mathcal{Y}_\Omega$, i.e.,

$$\mathcal{X}^{t+1} = \arg\min_{\mathcal{X}} \frac{\gamma}{2}\|\mathcal{L}^{t+1} - reshape(X_{(3)}D^{t+1})\|_F^2 + \frac{\rho}{2}\|\mathcal{X} - \mathcal{X}^t\|_F^2,$$

$$= \arg\min_{\mathcal{X}} \frac{\gamma}{2}\|L_{(3)}^{t+1} - X_{(3)}D^{t+1}\|_F^2 + \frac{\rho}{2}\|X_{(3)} - X_{(3)}^t\|_F^2, \tag{18}$$

$$= P_\Omega\left(ir\text{-}fold_3\left(\frac{\gamma L_{(3)}^{t+1} D^{\top t+1} + \rho X_{(3)}^t}{\gamma D^{t+1} D^{\top t+1} + \rho I}\right)\right),$$

where $ir\text{-}fold_3$ is an operator to re-array the stacked mode-3 fibers to the original spatio-irregular tensor $\mathcal{X}$ and P_Ω the projection onto $\{\mathcal{X} : \mathcal{X}_\Omega = \mathcal{Y}_\Omega\}$.

— Subproblem for updating $\mathcal{X}$ in SIR-TRPCA: The $\mathcal{X}$ subproblem is a typical least-square problem, i.e.,

$$\mathcal{X}^{t+1} = \arg\min_{\mathcal{X}} \frac{\gamma}{2}\|\mathcal{L}^{t+1} - reshape(X_{(3)}D^{t+1})\|_F^2 + \frac{\mu}{2}\|\mathcal{X} + \mathcal{S}^t - \mathcal{Y}\|_F^2 + \frac{\rho}{2}\|\mathcal{X} - \mathcal{X}^t\|_F^2,$$

$$= \arg\min_{\mathcal{X}} \frac{\gamma}{2}\|L_{(3)}^{\top t+1} - X_{(3))}D^{t+1}\|_F^2 + \frac{\mu}{2}\|X_{(3)} + S_{(3)}^t - Y_{(3)}\|_F^2 + \frac{\rho}{2}\|X_{(3)} - X_{(3)}^t\|_F^2, \tag{19}$$

$$= ir\text{-}fold_3\left(\frac{\gamma L_{(3)}^{t+1} D^{\top t+1} + \mu(Y_{(3)} - S_{(3)}^t) + \rho X_{(3)}^t}{\gamma D^{t+1} D^{\top t+1} + (\mu + \rho)I}\right),$$

where $ir\text{-}fold_3$ is to re-array the stacked mode-3 fibers as the original spatio-irregular tensor.

—Subproblem for updating $\mathcal{S}$ in SIR-TRPCA: The $\mathcal{S}$ subproblem is a typical soft thresholding problem [26], i.e.,

$$\mathcal{S}^{t+1} = \arg\min_{\mathcal{S}} \lambda\|\mathcal{S}\|_1 + \frac{\mu}{2}\|\mathcal{X}^{t+1} + \mathcal{S} - \mathcal{Y}\|_F^2 + \frac{\rho}{2}\|\mathcal{S} - \mathcal{S}^t\|_F^2,$$

$$= \mathsf{SOFT}\left(\frac{\mu(\mathcal{Y} - \mathcal{X}^{t+1}) + \rho\mathcal{S}}{\mu + \rho}, \frac{\lambda}{\mu + \rho}\right). \tag{20}$$

For a tensor $\mathcal{S}$, the corresponding soft thresholding operator can be defined as $\mathsf{SOFT}(\mathcal{S}, \tau)(\tau > 0)$ and $(\mathsf{SOFT}(\mathcal{S}, \tau))_{ijk} = \mathrm{sign}(\mathcal{S}_{ijk}) \max(|\mathcal{S}_{ijk}| - \tau, 0)$, where the sign function satisfies $\mathrm{sign}(\mathcal{S}_{ijk}) = 1$ when $\mathcal{S}_{ijk} > 0$, $\mathrm{sign}(\mathcal{S}_{ijk}) = 0$ when $\mathcal{S}_{ijk} = 0$, and $\mathrm{sign}(\mathcal{S}_{ijk}) = -1$ when $\mathcal{S}_{ijk} < 0$.

With the solution of each subproblem, we summarize the PAM-based algorithms for SIR-LRTC and SIR-TRPCA in Algorithms 1 and 2, respectively.

— *Time complexity analysis*: Here, we analyze the time complexities of the proposed method. The time complexity of the proposed method mainly comes from three aspects: (1) computing TSVD for updating $\mathcal{L}$; (2) updating transform D; (3) matrix product and inverse for updating $\mathcal{X}$. By assuming $\mathcal{L} \in \mathbb{R}^{\bar{n}_1 \times \bar{n}_2 \times n_3}$, $\mathcal{X}$ is a spatio-irregular tensor with n_3 frontal slices and l mode-3 fibers, and $D \in \mathbb{R}^{l \times \bar{n}_1 \bar{n}_2}$, we give the time complexity of the proposed method in Table 2.

— *Convergence guarantee*: Here, we establish the theoretical convergence for Algorithms 1 and 2. Since the key problem of establishing the convergence guarantee for both algorithms is

---

Algorithm 1: PAM for SIR-LRTC

Input The observed $\mathcal{Y}$, Ω, γ, ρ, $\bar{n}_1$, $\bar{n}_2$, ϵ, and t_{max}.
Output $\mathcal{X}$.
Initialize $\mathcal{X}^0$, D^0, $\mathcal{L}^0$, and $t = 0$ (see experimental setting for details).
While not converged and $t \leq t_{max}$ **do**
  Update $\mathcal{L}^{t+1}$ via Equation (16).
  Update D^{t+1} via Equation (17).
  Update $\mathcal{X}^{t+1}$ via Equation (18).
  Check the convergence condition:
  $\|\mathcal{X}^{t+1} - \mathcal{X}^t\|_F^2 / \|\mathcal{X}^t\|_F^2 \leq \epsilon$ or $t > t_{max}$.
  Let $t = t + 1$ and $\gamma = 1.2\gamma$.
End while

Algorithm 2: PAM for SIR-TRPCA

Input The observed $\mathcal{Y}$, γ, μ, λ, ρ, $\bar{n}_1$, $\bar{n}_2$, and ϵ.
Output $\mathcal{X}$.
Initialize $\mathcal{X}^0$, $\mathcal{S}^0$, D^0, $\mathcal{L}^0$, and $t = 0$ (see experimental setting for details).
While not converged and $t \leq t_{max}$ **do**
  Update $\mathcal{L}^{t+1}$ via Equation (16).
  Update $D_{(3)}^{t+1}$ via Equation (17).
  Update $\mathcal{X}^{t+1}$ via Equation (19).
  Update $\mathcal{S}^{t+1}$ via Equation (20).
  Check the convergence condition:
  $\|\mathcal{X}^{t+1} - \mathcal{X}^t\|_F^2 / \|\mathcal{X}^t\|_F^2 \leq \epsilon$ or $t > t_{max}$.
  Let $t = t + 1$, $\gamma = 1.2\gamma$, and $\mu = 1.2\mu$
End while

Table 2. Time Complexities of the Proposed Method

Subproblem	Time complexity
Update $\mathcal{L} \in \mathbb{R}^{\bar{n}_1 \times \bar{n}_2 \times n_3}$	$\mathcal{O}(\bar{n}_1 \bar{n}_2 n_3 \log n_3 + \min(\bar{n}_1, \bar{n}_2) \bar{n}_1 \bar{n}_2 n_3)$
Update $D \in \mathbb{R}^{l \times \bar{n}_1 \bar{n}_2}$	$\mathcal{O}(l\bar{n}_1 \bar{n}_2 n_3 + l^2 n_3 + l^3)$
Update $\mathcal{X}(X_{(3)} \in \mathbb{R}^{n_3 \times l})$	$\mathcal{O}(l\bar{n}_1 \bar{n}_2 n_3 + l^2 \bar{n}_1 \bar{n}_2 + l^3)$
Total	$\mathcal{O}(\bar{n}_1 \bar{n}_2 n_3 \log n_3 + \min(\bar{n}_1, \bar{n}_2) \bar{n}_1 \bar{n}_2 n_3 + l\bar{n}_1 \bar{n}_2 n_3 + l^2 (\bar{n}_1 \bar{n}_2 + n_3) + l^3)$

similar, we mainly establish the convergence guarantee for Algorithm 2 in detail. For SIR-TRPCA, define $\mathcal{Q} = \frac{\gamma}{2}\|\mathcal{L} - reshape(X_{(3)}D)\|_F^2 + \frac{\mu}{2}\|\mathcal{X} + \mathcal{S} - \mathcal{Y}\|_F^2$, $f_1 = \|\mathcal{L}\|_{\text{TNN}}$, $f_2 = \mathcal{C}_{\mathcal{X}}$, $f_3 = \lambda\|\mathcal{S}\|_1$, and $f_4 = \delta_{\mathcal{C}}(D)$, where $\mathcal{C}_{\mathcal{X}}$ is a constant. Then, the unconstrained SIR-TRPCA model (15) can be denoted by $f(\mathcal{L}, \mathcal{X}, \mathcal{S}, D) = \sum_{i=1}^4 f_i + \mathcal{Q}$.

THEOREM 3.5. *The sequence* $\{\mathcal{L}^t, \mathcal{X}^t, \mathcal{S}^t, D^t\}$ *generated by Algorithm 2 converges to a critical point of* $f(\mathcal{L}, \mathcal{X}, \mathcal{S}, D)$.

According to Attouch, Bolte, and Svaiter's paper [3], the proof of Theorem 3.5 is just verifying the following conditions hold in our setting, i.e.,

(1) f is a proper lower semi-continuous function;

(2) f satisfies the **Kurdyka-Łojasiewicz (K-Ł)** property;

(3) The sequence $\{\mathcal{L}^t, \mathcal{X}^t, \mathcal{S}^t, D^t\}$ satisfies the sufficient decrease condition and **relative error (RelErr)** condition.

Before verifying these conditions, we introduce some important preliminaries as follows.

Definition 3.6 (*K-Ł property [3]*). A proper lower semi-continuous function $f : \mathbb{R}^n \to \mathbb{R} \cup +\infty$ is said to have the K-Ł property at $\bar{x} \in dom(\partial f)$ if there exist $\eta \in (0, +\infty]$, a neighborhood U of $\bar{x}$, and a continuous concave function $\phi : [0, \eta) \to [0, +\infty)$ such that: (1) $\phi(0) = 0$; (2) ϕ is C^1 on $(0, \eta)$; (3) ϕ' is positive on $(0, \eta)$; (4) for each $x \in U \cap [f(\bar{x}) < f(x) < f(\bar{x}) + \eta]$, the K-Ł inequality hold: $\phi'(f(x) - f(\bar{x}))dist(0, \partial f(x)) \geq 1$.

LEMMA 3.7 (SUFFICIENT DECREASE [3]). *For functions $f_i(x_i)$ and function $\mathcal{Q}(x_1, x_2, \ldots, x_n)$, there exist $\rho > 0$, such that*

$$f_i(x_i^{t+1}) + \mathcal{Q}(x_1^{t+1}, \ldots, x_i^{t+1}, x_{i+1}^t, \ldots, x_n^t) + \frac{\rho}{2}\|x_i^{t+1} - x_i^t\|_F^2 \leq f_i(x_i^t) + \mathcal{Q}(x_1^{t+1}, \ldots, x_i^t, x_{i+1}^t, \ldots, x_n^t).$$
(21)

LEMMA 3.8 (RELERR [3]). *For functions $f_i(x_i)$ and function $\mathcal{Q}(x_1, x_2, \ldots, x_n)$, there exist $v_i^{t+1} \in \partial f_i(x_i^{t+1})$ and $\rho > 0$, such that*

$$\|v_i^{t+1} + \nabla_{x_i}\mathcal{Q}(x_1^{t+1}, \ldots, x_i^{t+1}, x_{i+1}^t, \ldots, x_n^t)\|_F \leq \rho\|x_i^{t+1} - x_i^t\|_F.$$
(22)

PROOF. Here, we begin to prove Theorem 3.5 by checking the three conditions inside of the theorem environment. Firstly, we prove that f is a proper lower semi-continuous function. It can verify that the summation of the Frobenius norm is a C^1 function with a locally Lipschitz continuous gradient. The l_1 norm is proper and lower semi-continuous. Since $\|\mathcal{L}\|_{\text{TNN}}$ is the summation of the nuclear norm of frontal slices from $\mathcal{L}$, TNN is proper and lower semi-continuous. Thus, f is a proper lower semi-continuous function.

Secondly, we prove that f satisfies the K-Ł property at each $\{\mathcal{L}^t, \mathcal{X}^t, \mathcal{S}^t, D^t\}$ by showing that f is a semi-algebraic function. The subset $\{D : \|D(:, j)\|_2 = 1\}$ is semi-algebraic. The l_1 norm, Frobenius norm, and TNN are semi-algebraic functions [19]. Thus, f is a semi-algebraic function. Since a semi-algebraic real-valued function is a K-Ł function, f has the K-Ł property at each $\{\mathcal{L}^t, \mathcal{X}^t, \mathcal{S}^t, D^t\}$ [5].

Thirdly, we prove that $\{\mathcal{L}^t, \mathcal{X}^t, \mathcal{S}^t, D^t\}$ satisfies the sufficient decrease condition and RelErr condition. For convenience, we denote variables $\{\mathcal{L}, \mathcal{X}, \mathcal{S}, D\}$ as $\{x_1, x_2, x_3, x_4\}$ and define $f_1 = \|\mathcal{L}\|_{\text{TNN}}$, $f_2 = \mathcal{C}_{\mathcal{X}}$, $f_3 = \lambda\|\mathcal{S}\|_1$, $f_4 = \delta_{\mathcal{C}}(D)$, and $\mathcal{Q} = \frac{\gamma}{2}\|\mathcal{L} - reshape(X_{(3)}D)\|_F^2 + \frac{\mu}{2}\|\mathcal{X} + \mathcal{S} - \mathcal{Y}\|_F^2$, where $\mathcal{C}_{\mathcal{X}}$ is a constant.

The proof of Lemma 3.7: Since each subproblem of f has the closed-form solution, let $\mathcal{L}^{k+1}$, $\mathcal{X}^{k+1}$, $\mathcal{S}^{k+1}$, G^{k+1}, and D^{k+1} are the optimal solutions of each subproblem of f, and then the sequence satisfies the sufficient decrease condition [3, 5].

The proof of Lemma 3.8: Before the proof of Lemma 3.8, we first prove the boundedness of $\mathcal{L}^t$ and $\mathcal{S}^t$. According to the sufficient decrease lemma, we conclude that

$$\|\mathcal{L}^t\|_{\text{TNN}} \leq f(\mathcal{L}^t, \mathcal{X}^{t-1}, \mathcal{S}^{t-1}, D^{t-1}) \leq \cdots \leq f(\mathcal{L}^0, \mathcal{X}^0, \mathcal{S}^0, D^0),$$
(23)

and

$$\|\mathcal{S}^t\|_1 \leq f(\mathcal{L}^t, \mathcal{X}^t, \mathcal{S}^t, D^{t-1}) \leq \cdots \leq f(\mathcal{L}^0, \mathcal{X}^0, \mathcal{S}^0, D^0).$$
(24)

Since $f(\mathcal{L}^0, \mathcal{X}^0, \mathcal{S}^0, D^0)$ is a constant, $\|\mathcal{S}^t\|_1$ and $\|\mathcal{L}^t\|_{\text{TNN}}$ are bounded. By the Cauchy–Schwarz inequality, we have

$$\|\mathcal{L}^t\|_F = \sum \|\bar{\mathcal{L}}^t(:,:,k)\|_F \le \sum \|\bar{\mathcal{L}}^t(:,:,k)\|_*, \tag{25}$$

and

$$\|\mathcal{S}^t\|_F^2 = \sum (s_{ijk}^t)^2 \le \left(\sum |s_{ijk}^t|\right)^2 = \|\mathcal{S}^t\|_1^2. \tag{26}$$

Thus, $\mathcal{L}^t$ and $\mathcal{S}^t$ are bounded. Since $\|D^t(:,j)\|_F = 1$, D^t is bounded. Then, since $\mathcal{L}^t$, $\mathcal{S}^t$, and D^t are bounded, $\mathcal{X}^t$ is bounded.

Now, we begin to prove Lemma 3.8. Let $\mathcal{L}^{t+1}, \mathcal{X}^{t+1}, \mathcal{S}^{t+1}$, and D^{t+1} are optimal solutions of subproblems of f and there exists subgradient for $f_1 = \|\mathcal{L}\|_{\text{TNN}}$ and $f_3 = \lambda\|\mathcal{S}\|_1$. We have that

$$0 \in \partial\|\mathcal{L}\|_{\text{TNN}} + \nabla_{\mathcal{L}} \mathcal{Q}(\mathcal{L}^{t+1}, \mathcal{X}^t, \mathcal{S}^t, D^t) + \rho(\mathcal{L}^{t+1} - \mathcal{L}^t), \tag{27}$$

and

$$0 \in \partial\|\mathcal{S}\|_1 + \nabla_{\mathcal{S}} \mathcal{Q}(\mathcal{L}^{t+1}, \mathcal{X}^{t+1}, \mathcal{S}^{t+1}, D^t) + \rho(\mathcal{S}^{t+1} - \mathcal{S}^t). \tag{28}$$

Let

$$v_1^{t+1} = -\nabla_{\mathcal{L}} \mathcal{Q} - \rho(\mathcal{L}^{t+1} - \mathcal{L}^t) \in \partial\|\mathcal{L}\|_{\text{TNN}}, \tag{29}$$

and

$$v_3^{t+1} = -\nabla_{\mathcal{S}} \mathcal{Q} - \rho(\mathcal{S}^{t+1} - \mathcal{S}^t) \in \partial\|\mathcal{S}\|_1. \tag{30}$$

Since $\nabla\mathcal{Q}$ Lipschitz continuous on any bounded set, there exist $\rho > 0$, such that

$$\|v_i^{t+1} + \nabla_{x_i}\mathcal{L}(x_1^{t+1}, \ldots, x_i^{t+1}, x_{i+1}^t, \ldots, x_4^t)\|_F \le \rho\|x_i^{t+1} - x_i^t\|_F, \tag{31}$$

The proof of the RelErr condition is completed.

Satisfying the three key conditions in [5] and [3], we can conclude that the bounded sequence $\{\mathcal{L}^t, \mathcal{X}^t, \mathcal{X}^t, D^t\}$ converges to a critical point of f. The proof for Algorithm 1 is similar to the proof process of Algorithm 2. □

4 Experiments

Here, we evaluate the performance of the proposed SIR-LRTC and SIR-TRPCA by setting synthetic and real-world spatio-irregular tensor imputation and denoising experiments. Our target is to recover the high-quality $\mathcal{X}$ from the observed corrupted data $\mathcal{Y}$. Two metrics served as the numerical performance evaluation, including the RelErr and **peak signal-to-noise ratio (PSNR)**, which are formulated as

$$\text{RelErr} = \frac{\|\mathcal{X} - \mathcal{X}_t^*\|_F}{\|\mathcal{X}^*\|_F},$$

and

$$\text{PSNR} = 10 \log_{10} \frac{ln_3 \max(\mathcal{X}_t^*)^2}{\|\mathcal{X} - \mathcal{X}^*\|_F^2},$$

where $\mathcal{X}^*$ is the original spatio-irregular tensor with n_3 frontal slices and l mode-3 fibers.

Competing Methods: Since there are no fundamental tensor decompositions designed for spatio-irregular tensors, we consider the classical tensor-based method TNN and low-rank matrix factorization with preprocessing as competing methods.

For the TNN-based method, we first convert the spatio-irregular tensor to a regular tensor by using zero-padding, interpolation, and element-wise 0-1 weighting, and then apply the classical tensor-based method TNN (termed as TNN-Z, TNN-I, and TNN-W, respectively). Specifically, in

the TNN-I method, we transform the spatio-irregular tensor into a regular tensor by estimating the entries of the complement of the incomplete 2D grid with the MATLAB built-in function "griddata,"[1] which is also used as the preprocessing in the community (e.g., [41]). In the TNN-W method, we can transform the spatio-irrgular tensor into a regular tensor $\mathcal{W} \odot \mathcal{X}$ by using the element-wise 0-1 weighting, where $\mathcal{W}_{ijk} = 1$ indicates the corresponding $\mathcal{X}_{ijk}$ belongs to the original spatio-irregular tensor, $\mathcal{W}_{ijk} = 0$ indicates the corresponding $\mathcal{X}_{ijk}$ doesn't belong to the original spatio-irregular tensor, and $\odot$ is the Hadamard product. Then, the resulting regular tensor $\mathcal{W} \odot \mathcal{X}$ can be tackled by classical TNN minimization-based imputation and denoising models and alternating direction method of multipliers can be considered to solve the corresponding convex optimization problems [26, 48].

For low-rank matrix factorization-based method, we first transform the spatio-irregular tensor into a matrix by the mode-3 matricization of the spatio-irregular tensor, and then use the **non-negative low-rank matrix factorization (NLRMF)** method [22]. To impute the missing values of the spatio-irregular tensor in the NLRMF method, we introduce the constraint $\mathcal{Y}_\Omega = \mathcal{X}_\Omega$ to the NLRMF method, where $\mathcal{Y}$ is the observed spatio-irregular tensor, $\mathcal{X}$ is the underlying spatio-irregular tensor from $\mathcal{Y}$, and the constraint $\mathcal{Y}_\Omega = \mathcal{X}_\Omega$ enforces the entries of $\mathcal{X}$ in index Ω equal to the corresponding entries of the observation $\mathcal{Y}$. To remove sparse noise of the spatio-irregular tensor in the NLRMF method, we introduce the constraint $\mathcal{Y} = \mathcal{X} + \mathcal{S}$ to the NLRMF method, where $\mathcal{Y}$ is the observed spatio-irregular tensor, $\mathcal{X}$ is the denoised spatio-irregular tensor from $\mathcal{Y}$, and $\mathcal{S}$ is the sparse noise. The source codes of TNN and NLRMF were downloaded from the links.[2,3]

Parameters Setting: All methods are tuned for the highest PSNR value by using the grid search method. In the imputation experiment, for SIR-LRTC, $\bar{n}_1$ and $\bar{n}_2$ are selected from $\{10, 15, ..., 50\}$, ρ is fixed as 0.001, and $\gamma = (1-\tau\rho)/\tau$, where τ is selected from $\{0.07, 0.09, 0.1, 0.3, 0.5, 0.7, 0.9, 1, 3, 5, 7, 9\}$. For TNN-Z, TNN-I, and TNN-W in the imputation experiment, μ is selected from $\{0.01, 0.05, 0.1, 0.5, 1, 5, 10, 50, 100\}$. For NLRMF in the imputation experiment, r is selected from $\{1, 2, \ldots, \lceil \min(n_3, l)/2 \rceil\}$ for the spatio-irregular tensor with n_3 frontal slices and l mode-3 fibers. In the denoising experiment, for SIR-TRPCA, $\bar{n}_1$ and $\bar{n}_2$ are selected from $\{10, 15, ..., 50\}$, μ is selected from $\{0.01, 0.1, 1, 10, 100\}$, λ is selected from $\{0.01, 0.03, 0.05, 0.07, 0.1, 0.3, 0.5, 0.7\}$, ρ is fixed as 0.001, and $\gamma = (1 - \tau\rho)/\tau$, where τ is selected from $\{0.07, 0.09, 0.1, 0.3, 0.5, 0.7, 0.9, 1, 3, 5, 7, 9\}$. For TNN-Z, TNN-I, and TNN-W in the denoising experiment, μ is selected from $\{0.01, 0.05, 0.1, 0.5, 1, 5, 10, 50, 100\}$ and λ is selected from $\{0.01, 0.03, 0.05, 0.07, 0.1, 0.3, 0.5, 0.7\}$. For NLRMF in the denoising experiment, r is selected from $\{1, 2, \ldots, \lceil \min(n_3, l)/2 \rceil\}$ for the spatio-irregular tensor with n_3 frontal slices and l mode-3 fibers, μ is selected from $\{0.01, 0.05, 0.1, 0.5, 1, 5, 10, 50, 100\}$, and λ is selected from $\{0.01, 0.03, 0.05, 0.07, 0.1, 0.3, 0.5, 0.7\}$.

Initialization: Since the proposed method is strongly nonconvex, the initialization is important to its performance. $\mathcal{X}^0$ is initialized by the proposed method with the fixed transform $\mathbf{D}$. Specifically, we fix $\mathbf{D}$ as the DCT-based matrix and let $\mathcal{X}^0$ be equal to the observation $\mathcal{Y}$, and then we implement our method without updating $\mathbf{D}$ to obtain an initial result $\tilde{\mathcal{X}}$. Subsequently, we use the DCT-based matrix as the initialized $\mathbf{D}^0$ and $\tilde{\mathcal{X}}$ as the initialized $\mathcal{X}^0$ and then implement Algorithms 1 and 2, where $\mathcal{L}^0 = reshape(\mathbf{D}^0_{(3)} \mathbf{X}^0)$ and the initialized $\mathcal{S}^0$ in Algorithm 2 is a tensor with all values be zero.

Implementation Details: The programming language is Matlab for all methods. All methods are implemented in Matlab R2019a on a desktop computer, which equips an Intel Core i9-10900KF 3.70-GHz CPU (All 10 computational cores were allowed to be used) and 256 GB RAM.

---

[1]https://www.mathworks.com/help/matlab/ref/griddata.html
[2]TNN: https://github.com/canyilu/Tensor-tensor-product-toolbox
[3]NLRMF: https://github.com/hiroyuki-kasai/NMFLibrary

Table 3. The Basic Information of Superpixels from the Color Image *Butterfly* and MSI *Pompoms*

Data	Superpixel	Size			Number of mode-3 fibers
		n_1	n_2	n_3	l
Butterfly		37	39	3	735
		35	45	3	495
Pompoms		39	34	31	808
		49	46	31	1196

Note: The n_1 and n_2 represent the height and width of the smallest rectangle containing the spatial domain of the spatio-irregular tensor, and n_3 is the number of the fontal slices of the spatio-irregular tensor.

Synthetic Examples: In this experiment, we consider the superpixel from the color image *Butterfly* and **multispectral image (MSI)** *Pompoms* as synthetic spatio-irregular tensors. The color image "*Butterfly*" is part of the public Leeds butterfly dataset,[4] and the MSI "*Pompoms*" is part of the public CAVE MSI dataset.[5] For visualization of superpixels from the MSI Pompoms, we use band 30 as the red channel, band 10 as the green channel, and band 20 as the blue channel to obtain a pseudo-RGB image. Table 3 lists the basic information about these spatio-irregular tensors, including their size and the number of mode-3 fibers. We compare the performance of the proposed method and competing methods on imputation and denoising tasks. In the imputation task, we uniformly sample elements from the matrix formed by the mode-3 fibers of the spatio-irrgular tensor to generate the observed data by using the MATLAB built-in function "randsample," and the sampling rate is set as 0.2 for the color image and is set as 0.1 for MSI. In the denoising task, salt and pepper noise with the ratio = 0.3 is added to the matrix formed by the mode-3 fibers of the spatio-irrgular tensor to generate the observed data.

Tables 4 and 5 give numerical results by different methods for superpixel imputation and denoising tasks. The proposed SIR-LRTC and SIR-TRPCA significantly outperform other competing methods in terms of the RelErr and PSNR values for the selected superpixels on different tasks. Since there are only three bands for the color image, stacking mode-3 fibers as a matrix is near failure in the imputation task. For MSI superpixels, NLRMF performs well because the third mode of MSI has abundant information. The proposed method is superior to other methods on both MSI and color image because the proposed method fully exploits the spatial and spectral correlation.

Figures 6 and 7 show the visual results by different methods. In Figure 6, we can see that TNN-Z and TNN-W lead to significant artifacts because preprocessing methods inevitably introduce bias information. The proposed method removes almost all of the salt and pepper noise while maintaining the details of the superpixels as compared with other methods. The underlying mechanism is that the proposed method uses the learnable spatial transform to project the original spatio-irregular

---

Table 4. The Numerical Results by Different Methods for Superpixel Imputation and Denoising Tasks

Imputation (Sampling rate = 0.2)							
Superpixel	Metrics	Observed	NLRMF	TNN-Z	TNN-I	TNN-W	SIR-LRTC
	RelErr	0.8998	0.7790	0.6346	0.5687	0.6324	**0.4559**
	PSNR	15.06	16.35	18.15	19.08	18.17	**21.00**
	RelErr	0.8963	0.7706	0.4496	0.4980	0.6604	**0.2415**
	PSNR	10.84	12.16	16.88	15.95	13.54	**22.24**
Denoising (Salt and pepper noise ratio = 0.3)							
Superpixel	Metrics	Observed	NLRMF	TNN-Z	TNN-I	TNN-W	SIR-TRPCA
	RelErr	1.0420	0.4410	0.4228	0.3530	0.4283	**0.2876**
	PSNR	13.82	21.29	21.66	23.22	21.54	**25.00**
	RelErr	0.5636	0.3656	0.4114	0.1919	0.4197	**0.1670**
	PSNR	14.88	18.64	17.61	24.23	17.44	**25.44**

Here, the superpixels are from the color image *Butterfly*. Bold indicates the best numerical results.

Table 5. The Numerical Results by Different Methods for Superpixel Imputation and Denoising Tasks

Imputation (Sampling rate = 0.1)							
Superpixel	Metrics	Observed	NLRMF	TNN-Z	TNN-I	TNN-W	SIR-LRTC
	RelErr	0.9491	0.2111	0.0985	0.0985	0.1322	**0.0932**
	PSNR	11.25	24.31	30.92	30.93	28.37	**31.40**
	RelErr	0.9498	0.4423	0.3147	0.2496	0.2991	**0.2284**
	PSNR	16.73	23.37	26.32	28.34	26.77	**29.11**
Denoising (Salt and pepper noise ratio = 0.3)							
Superpixel	Metrics	Observed	NLRMF	TNN-Z	TNN-I	TNN-W	SIR-TRPCA
	RelErr	1.0319	0.0485	0.0740	0.0566	0.0686	**0.0369**
	PSNR	10.52	37.07	33.41	35.74	34.06	**39.45**
	RelErr	3.3540	0.2319	0.1941	0.2602	0.1966	**0.0453**
	PSNR	5.7706	28.98	30.52	27.98	30.41	**37.66**

Here, the superpixels are from the MSI *Pompoms*. Bold indicates the best numerical results.

tensor into a latent regular tensor while preserving the essential low-rankness of the spatio-irregular tensor without introducing extra bias information. In Figure 7, we can observe that NLRMF leads to color distortion while the proposed SIR-LRTC successfully fills the missing area and preserves color fidelity. In summary, our method is more suitable for diverse tasks of spatio-irregular tensors.

Real-World Examples: In this experiment, we test the performance of the proposed methods on real-world spatio-irregular tensors. We mainly compare the performance of the proposed method and competing methods on spatial transcriptomics data imputation and HSI denoising. Here, to

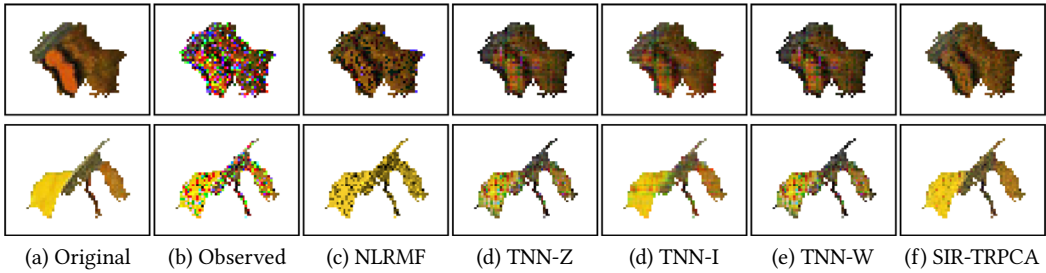(a) Original   (b) Observed   (c) NLRMF   (d) TNN-Z   (d) TNN-I   (e) TNN-W   (f) SIR-TRPCA

Fig. 6. The visual results by different methods for superpixel denoising. Here, the superpixels are from the color image *Butterfly* and corrupted by salt and pepper noise with the ratio = 0.3.

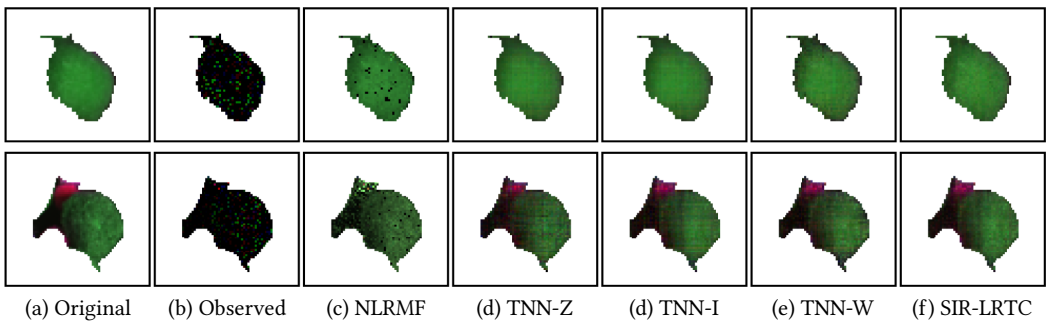(a) Original   (b) Observed   (c) NLRMF   (d) TNN-Z   (d) TNN-I   (e) TNN-W   (f) SIR-LRTC

Fig. 7. The visual results by different methods for superpixel imputation. Here, the superpixels are from the MSI *Pompoms* and the sampling rate is 0.1. For visualization of superpixels from the MSI Pompoms, we use band 30 as the red channel, band 10 as the green channel, and band 20 as the blue channel to obtain a pseudo-RGB image.

comprehensively evaluate the performance of different methods, we not only compared their recovery results but also further compared their influence on downstream applications.

Spatial Transcriptomics Data Imputation: Spatial transcriptomics technology enables high-throughput collection of gene expression coupled with spatial information in biological tissues. Such data is a typical kind of spatio-irregular multidimensional data. The gene expression of each spot is measured, where the spots are spatially distributed on some tissue slice with irregular boundary. An important characteristic of such data is its high proportion of zero entries, which includes the true zero expression entries and missing values ("dropout"). Here, we applied the proposed method to spatial transcriptomics data of the human heart tissue [2] (see its visualization in 2D from Figure 8). Table 6 lists the basic information of this spatio-irregular tensor, including its size and the number of mode-3 fibers. Since there is no true reference of the data, for performance evaluation, we consider the non-zero values of the gene expression as the true reference, and uniformly sample 30% elements from the non-zero values to generate the observation.

Table 7 gives numerical results by different methods for spatial transcriptomics data imputation. The proposed SIR-LRTC significantly outperforms other competing methods in terms of the RelErr and PSNR values. Specifically, SIR-LRTC decreases around 10% RelErr as compared with the second-best method.

Figure 9 shows clustering results of spatial transcriptomics data imputed by different methods. Specifically, we use classical *K*-means [30] to cluster the spatial transcriptomics data imputed by different methods and then reduce the dimensionality of the imputed spatial transcriptomics

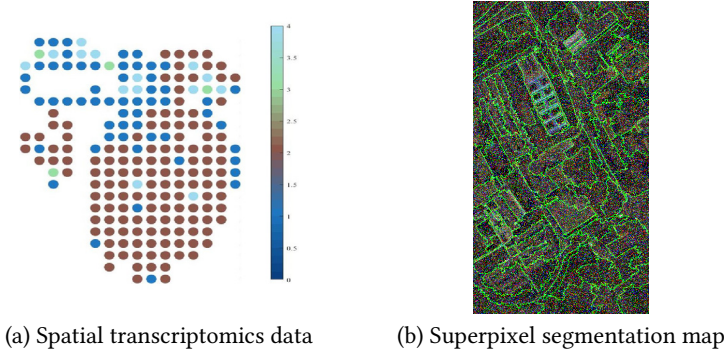(a) Spatial transcriptomics data   (b) Superpixel segmentation map

Fig. 8. Spatio-irregular tensors from the real world. (a) The spatial transcriptomics data of the human heart tissue visualized in 2D. (b) The superpixel segmentation map of the noisy HSI *Pavia University*.

Table 6.   The Basic Information of the Spatial Transcriptomics Data

Data	Size			Number of mode-3 fibers
	n_1	n_2	n_3	l
Human heart tissue	22	16	250	210

Note: The n_1 and n_2 represent the height and width of the smallest rectangle containing the spatial domain of the spatio-irregular tensor, and n_3 is the number of the fontal slices of the spatio-irregular tensor.

Table 7.   The Numerical Results by Different Methods for Spatial Transcriptomics Data Imputation

Metrics	Observed	NLRMF	TNN-Z	TNN-I	TNN-W	SIR-LRTC
RelErr	0.8370	0.5275	0.4969	0.5006	0.5518	**0.4271**
PSNR	31.04	35.05	35.57	35.50	34.66	**36.89**

Bold indicates the best numerical results.

data by t-SNE [29] for visualization in 2D. We also consider the mean silhouette score [34] to quantitatively measure clustering results, where the higher value indicates the better clustering result. As observed from Figure 9, the clustering result of spatial transcriptomics data imputed by our method shows better grouping of similar classes and better separation of different classes and achieves the best mean silhouette score numerically. In summary, our method can benefit downstream clustering as compared with competing methods.

HSI Denoising: Superpixel segmentation has been developed to be a promising tool for feature extraction of HSI [46]. Here, we divide an HSI as many superpixels for the HSI denoising task, where each superpixel of the HSI is a spatio-irregular tensor. *Pavia University*[6] is employed as the test data, which is of size $610 \times 340 \times 103$. For visualization of this HSI, we can use band 55 as the red channel, band 41 as the green channel, and band 12 as the blue channel to obtain a pseudo-RGB image. Salt and pepper noise with the ratio = 0.3 is added to all bands of the image. This data is

---

[6]Available at https://www.ehu.eus/ccwintco/index.php?title=Hyperspectral_Remote_Sensing_Scenes
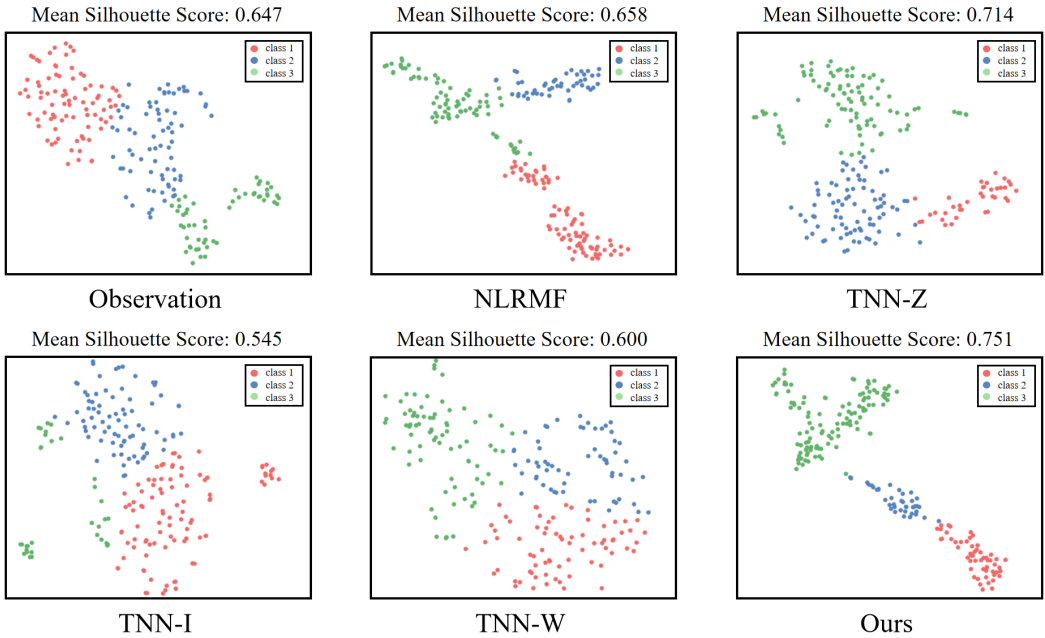
Fig. 9. Clustering results of spatial transcriptomics data imputed by different methods. Here, we use classical K-means to cluster the spatial transcriptomics data imputed by different methods and then reduce the dimensionality of the imputed spatial transcriptomics data by t-SNE for visualization in 2D. The mean silhouette score is employed to numerically measure the similarity of objects in a class, where the higher value indicates the better clustering.

Table 8. The Numerical Results by Different Methods for HSI *Pavia University* Denoising

Metrics	Observed	NLRMF	TNN-Z	TNN-I	TNN-W	SIR-TRPCA
RelErr	1.609	0.0799	0.1439	0.1099	0.1446	**0.0560**
PSNR	14.32	40.41	35.30	37.64	35.26	**43.51**

Bold indicates the best numerical results.

subdivided into 80 superpixels by using the entropy rate superpixel segmentation method [25]. We give the superpixel segmentation map of the noisy *Pavia University* in Figure 8. For performance evaluation, we first compose the denoised superpixels into a holistic image and then compute the RelErr and PSNR on the holistic image.

Table 8 gives numerical results by different methods for HSI *Pavia University* denoising. The proposed SIR-TRPCA significantly outperforms other competing methods in terms of the RelErr and PSNR values. Figure 10 shows visual results by different methods, and each subfigure in this Figure is a composite of corresponding denoised superpixels. We can observe that all compared methods successfully remove almost all of the salt and pepper noise because considering the superpixel as the basic unit of the HSI can fully exploit the local correlation of the HSI.

Furthermore, Figure 11 shows the classification map and accuracy of denoised HSI by different methods. Specifically, we use the **support vector machine (SVM)** as the classifier [31]. We can observe that the classification result of denoised HSI by the proposed SIR-TRPCA is mostly close to the ground truth as compared with other methods. In summary, our method can benefit downstream classification as compared with competing methods.

(a) Original   (b) Observed   (c) NLRMF   (d) TNN-Z   (d) TNN-I   (e) TNN-W   (f) SIR-TRPCA
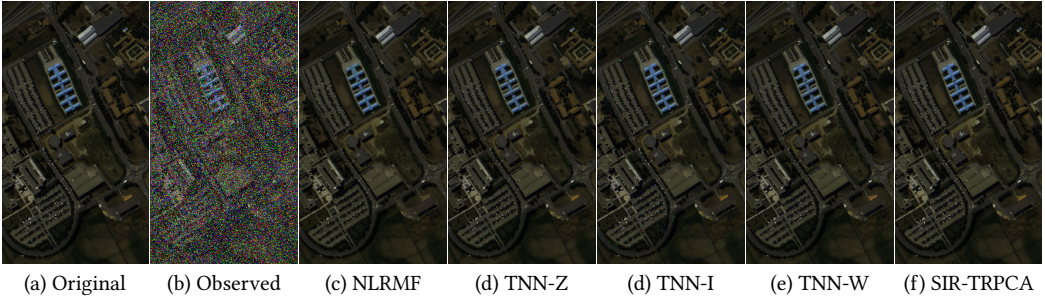
Fig. 10. The visual results by different methods for HSI *Pavia University* denoising. Here, this HSI is corrupted by salt and pepper noise with the ratio = 0.3. Each subfigure in this Figure is a composite of corresponding denoised superpixels. For visualization of this HSI, we use band 55 as the red channel, band 41 as the green channel, and band 12 as the blue channel to obtain a pseudo-RGB image.
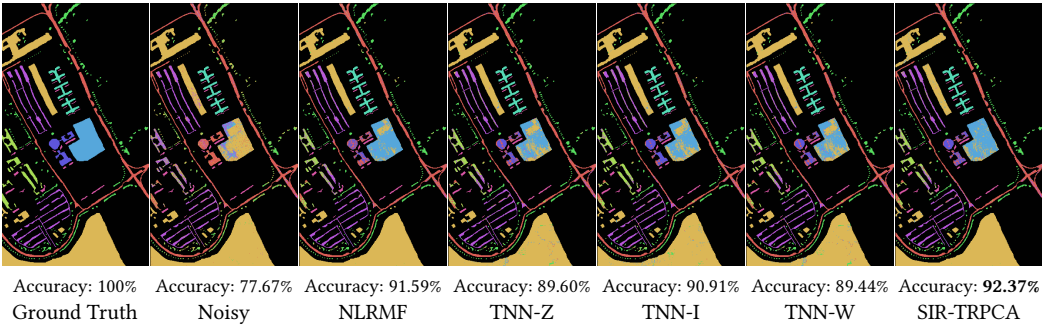

Accuracy: 100%   Accuracy: 77.67%   Accuracy: 91.59%   Accuracy: 89.60%   Accuracy: 90.91%   Accuracy: 89.44%   Accuracy: **92.37%**
Ground Truth   Noisy   NLRMF   TNN-Z   TNN-I   TNN-W   SIR-TRPCA

Fig. 11. Classification map and accuracy of denoised HSI by different methods on *Pavia University*. Here, we use the SVM as the classifier.

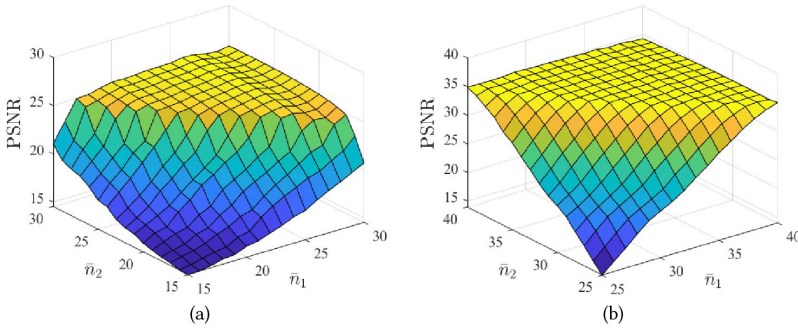(a)   (b)

Fig. 12. The numerical results of the proposed method with varying $\bar{n}_1$ and $\bar{n}_2$ for superpixel denoising of different data. Here, (a) is the result of the superpixel from the color image *Butterly*; (b) is the result of the superpixel from the MSI *Pompoms*.

Discussion for the Influence of the Spatial Size of the Latent Spatio-Regular Tensor: The key of our method is using the learnable transform to project the original spatio-irregular tensor into its latent spatio-regular tensor. The parameters $\bar{n}_1$ and $\bar{n}_2$ determine the spatial size of the latent spatio-regular tensor. To analyze the influence of $\bar{n}_1$ and $\bar{n}_2$, we test the proposed method with varying $\bar{n}_1$ and $\bar{n}_2$. Figure 12 shows the numerical results of the proposed method with varying $\bar{n}_1$

and $\bar{n}_2$ for superpixel denoising of different data. We can find that the performance of our method becomes robust when $\bar{n}_1\bar{n}_2$ is larger than a threshold. Here, the threshold is usually the total number of mode-3 fibers of the spatio-irregular tensor. Moreover, we can see that $\bar{n}_1$ and $\bar{n}_2$ of the latent regular tensor are usually smaller than n_1 and n_2 of the original spatio-irregular tensor.

5 Conclusion

In this article, we proposed a fundamental tensor decomposition LTA-TSVD for emerging spatio-irregular tensors, which allows us to leverage the intrinsic structure behind the spatio-irregular tensor. Based on LTA-TSVD, we developed SIR-LRTC and SIR-TRPCA models for spatio-irregular tensor imputation and denoising and designed corresponding solving algorithms for resulting models with theoretical convergence. Extensive synthetic and real experiments show the proposed method outperforms other competing approaches in imputation and denoising tasks and benefits downstream applications.

References

[1] A. Afshar, I. Perros, H. Park, C. deFilippi, X. Yan, W. Stewart, J. Ho, and J. Sun. 2020. TASTE: Temporal and static tensor factorization for phenotyping electronic health records. In *Proc. ACM Conf. Health Inference Learn,* 193–203.

[2] M. Asp, S. Giacomello, C. Wu, D. Furth, X. Qian, E. Wardell, J. Custodio, J. Reimegard, F. Salmen, et al. 2019. A spatiotemporal organ-Wide gene expression and cell atlas of the developing human heart. *Cell* 179, 7 (2019), 1647–1660.

[3] H. Attouch, J. Bolte, and B. F. Svaiter. 2013. Convergence of descent methods for semi-algebraic and tame problems: Proximal algorithms, forward-backward splitting, and regularized Gauss-Seidel methods. *Math. Program.* 137, 1 (2013), 91–129.

[4] J. A Bengua, H. N. Phien, H. D. Tuan, and M. N. Do. 2017. Efficient tensor completion for color image and video recovery: Low-rank tensor train. *IEEE Trans. Image Process.* 26, 5 (2017), 2466–2479.

[5] J. Bolte, S. Sabach, and M. Teboulle. 2014. Proximal alternating linearized minimization for nonconvex and nonsmooth problems. *Math. Program.* 46, 1 (2014), 459–494.

[6] J.-F. Cai, E. J. Candes, and Z. Shen. 2010. A singular value thresholding algorithm for matrix completion. *SIAM J. Optim.* 20 (2010), 1956–1982.

[7] Y. Chang, L. Yan, X.-L. Zhao, H. Fang, Z. Zhang, and S. Zhong. 2020. Weighted low-rank tensor recovery for hyperspectral image restoration. *IEEE Trans. Cybern.* (2020), 1–15.

[8] D. Chu, W. Shi, S. Eswar, and H. Park. 2021. An alternating rank-k nonnegative least squares framework (ARKNLS) for nonnegative matrix factorization. *SIAM J. Matrix Anal. Appl.* 42 (2021), 1451–1479.

[9] A. Cichocki, N. Lee, I. Oseledets, A. Phan, Zhao Q, and D. P. Mandic. 2016. Tensor networks for dimensionality reduction and large-scale optimization: Part 1 low-rank tensor decompositions. *Found. Trends Mach. Learn.* 9 (2016), 249–429.

[10] A. Cichocki, A. H. Phan, Q. Zhao, N. Lee, I. Oseledets, M. Sugiyama, and D. P. Sugiyama. 2019. Tensor networks for dimensionality reduction and large-scale optimization: Part 2 applications and future perspectives. *Found. Trends Mach. Learn.* 9 (2019), 431–673.

[11] D. M. Dunlavy, T. G. Kolda, and E. Acar. 2011. Temporal link prediction using matrix and tensor factorizations. *ACM Trans. Knowl. Discov. Data* 5, 2 (2011), 1–27, Art no: 10.

[12] E. Gujral and E. E. Papalexakis. 2022. APTERA: automatic PARAFAC2 tensor analysis. In *Proc. IEEE Int. Conf. Adv. Soc. Netw. Anal. Min. (ASONAM)*, 17–21.

[13] R. A. Harshman. 1972. PARAFAC2: Mathematical and technical notes. *UCLA Working Pap. Phonetics* 22 (1972), 30–47.

[14] C. J. Hillar and L.-H. Lim. 2013. Most tensor problems are NP-hard. *J. ACM* 60, 6 (2013), 1–39.

[15] L. Hitchcock. 1927. The expression of a tensor or a polyadic as a sum of products. *J. Math. Phys.* 6 (1927), 164–189.

[16] Y. Hu and B. B. Work. 2020. Robust tensor recovery with fiber outliers for traffic events. *ACM Trans. Knowl. Discov. Data* 15, 1 (2020), 1–25, Article no. 6.

[17] T.-X. Jiang, M. K. Ng, J. Pan, and G.-J. Song. 2023. Nonnegative low rank tensor approximations with multidimensional image applications. *Numer. Math.* 153, 1 (2023), 141–170.

[18] T.-X. Jiang, M. K. Ng, X.-L. Zhao, and T.-Z. Huang. 2020. Framelet representation of tensor nuclear norm for third-order tensor completion. *IEEE Trans. Image Process.* 29 (2020), 7233–7244.

[19] T.-X. Jiang, X.-L. Zhao, H. Zhang, and M. K. Ng. 2023. Dictionary learning with low-rank coding coefficients for tensor completion. *IEEE Trans. Neural Netw. Learn. Syst.* 34, 2 (2023), 932–946.

[20] T.-X. Jiang, L. Zhuang, T.-Z. Huang, X.-L. Zhao, and J. M. Bioucas-Dias. 2022. Adaptive hyperspectral mixed noise removal. *IEEE Trans. Geosci. Remote Sens.* 60 (2022), 1–13.

[21] M. E Kilmer and C. D. Martin. 2011. Factorization strategies for third-order tensors. *Linear Algebra. Appl.* 435, 3 (2011), 641–658.

[22] D. D. Lee and H. S. Seung. 2000. Algorithms for non-negative matrix factorization. In *Proc. Neural Inf. Process. Syst. (NIPS)*, 535–541.

[23] L. Lin, K. Wang, D. Meng, W. Zuo, and L. Zhang. 2018. Active self-paced learning for cost-effective and progressive face identification. *IEEE Trans. Pattern Anal. Mach. Intell.* 40, 1 (2018), 7–19.

[24] J. Liu, M. Przemyslaw, W. Peter, and J. Ye. 2013. Tensor completion for estimating missing values in visual data. *IEEE Trans. Pattern Anal. Mach. Intell.* 35, 1 (2013), 208–220.

[25] M.-Y. Liu, S. Ramalingam O. Tuzel, and R. Chellappa. 2011. Entropy rate superpixel segmentation. In *Proc. IEEE Conf. Comput. Vis. Pattern Recognit. (CVPR)*, 2097–2104.

[26] C. Lu, J. Feng, Y. Chen, W. Liu, Z. Lin, and S. Yan. 2020. Tensor robust principal component analysis with a new tensor nuclear norm. *IEEE Trans. Pattern Anal. Mach. Intell.* 42, 4 (2020), 925–938.

[27] C. Lu, X. Peng, and Y. Wei. 2019. Low-rank tensor completion with a new tensor nuclear norm induced by invertible linear transforms. In *Proc. IEEE Conf. Comput. Vis. Pattern Recognit. (CVPR)*, 5996–6004.

[28] Y.-S. Luo, X.-L. Zhao, Z. Li, M. K. Ng, and D. Meng. 2024. Low-rank tensor function representation for multi-dimensional data recovery. *IEEE Trans. Pattern Anal. Mach. Intell.* 46, 5 (2024), 3351–3369.

[29] L. V. D. Maaten and G. E. Hinton. 2008. Visualizing data using t-SNE. *J. Mach. Learn. Res.* 9 (2008), 2579–2605.

[30] J. MacQueen. 1967. Some methods for classification and analysis of multivariate observations. In *Proc. 5th Berkeley Symp. Math. Statist. Probab.,* 281–297.

[31] F. Melgani and L. Bruzzone. 2004. Classification of hyperspectral remote sensing images with support vector machines. *IEEE Trans. Geosci. Remote Sens.* 42, 8 (2004), 1778–1790.

[32] I. V. Oseledets. 2011. Tensor-train decomposition. *SIAM J. Sci. Comput.* 33 (2011), 2295–2317.

[33] E. E. Papalexakis, C. Faloutsos, and N. D. Sidiropoulos. 2015. ParCube: Sparse parallelizable CANDECOMP-PARAFAC tensor decomposition. *ACM Trans. Knowl. Discov. Data* 10, 1 (2015), 1–25, Artcile no. 3.

[34] P. J. Rousseeuw. 1987. Silhouettes: A graphical aid to the interpretation and validation of cluster analysis. *J. Comput. Appl. Math.* 20 (1987), 53–65.

[35] Q. Song, H.Ge, J. Caverlee, and X. Hu. 2019. Tensor completion algorithms in big data analytics. *ACM Trans. Knowl. Discov. Data* 13, 1 (2019), 1–48, Article no. 6.

[36] L. R Tucker. 1966. Some mathematical notes on three-mode factor analysis. *Psychometrika* 31, 3 (1966), 279–311.

[37] H. Wang, F. Zhang, J. Wang, T. Huang, J. Huang, and X. Liu. 2022. Generalized nonconvex approach for low-tubal-rank tensor recovery. *IEEE Trans. Neural Netw. Learn. Syst.* 33, 8 (2022), 3305–3319.

[38] J. Wang, J. Cai, Y. Shi, and B. Yin. 2016. Incoherent dictionary learning for sparse representation based image denoising. *Appl. Comput. Harmon. Anal.* 41, 1 (2016), 94–138.

[39] W. Wang and M. K. Ng. 2021. Color image restoration by saturation-value total variation regularization onvector bundles. *SIAM J. Imaging Sci.* 12 (2021), 178–197.

[40] Y. Xu, R. Hao, W. Yin, and Z. Su. 2015. Parallel matrix factorization for low-rank tensor completion. *Inverse Probl. Imaging* 9, 2 (2015), 601–624.

[41] N. Yair and T. Michaeli. 2018. Multi-scale weighted nuclear norm image restoration. In *Proc. IEEE Conf. Comput. Vis. Pattern Recognit. (CVPR)*, 3165–3174.

[42] J. Yu, C. Li, Q. Zhao, and G. Zhou. 2019. Tensor-ring nuclear norm minimization and application for visual data completion. In *Proc. IEEE Int. Conf. Acoust. Speech Signal Process. (ICASSP),* 3142–3146.

[43] Q. Yuan, L. Zhang, and H. Shen. 2012. Hyperspectral image denoising employing a spectral-spatial adaptive total variation model. *IEEE Trans. Geosci. Remote Sens.* 50, 10 (2012), 3660–3677.

[44] H. Zhang, J. Li, Y. Huang, and L. Zhang. 2014. A nonlocal weighted joint sparse representation classification method for hyperspectral imagery. *IEEE J. Sel. Topics Appl. Earth Observ. Remote Sens.* 7, 6 (2014), 2056–2065.

[45] H. Zhang, H. Zhai, L. Zhang, and P. Li. 2016b. Spectral-spatial sparse subspace clustering for hyperspectral remote sensing images. *IEEE Trans. Geosci. Remote Sens.* 54, 6 (2016), 3672–3684.

[46] S. Zhang, T. Lu, W. Fu, and S. Li. 2022. Superpixel-level hybrid discriminant analysis for hyperspectral image feature extraction. *IEEE Trans. Geosci. Remote Sens.* 60 (2022), 1–13, Article no. 5540713.

[47] X. Zhang, Q. Shen, Y. Chen, G. Zhang, Z. Hua, and J. Su. 2023. Multi-view ensemble clustering via low-rank and sparse decomposition: from matrix to tensor. *ACM Trans. Knowl. Discov. Data* 17, 7 (2023), 1–19, Article no. 103.

[48] Z. Zhang and S. Aeron. 2017. Exact tensor completion using t-SVD. *IEEE Trans. Signal Process.* 65, 6 (2017), 1511–1526.

[49] Z. Zhang, G. Ely, S. Aeron, N. Hao, and M. Kilmer. 2014. Novel methods for multilinear data completion and de-noising based on tensor-SVD. In *Proc. IEEE Conf. Comput. Vis. Pattern Recognit. (CVPR)*, 3842–3849.

[50] Z. Zhang, E. Pasolli, M. M. Crawford, and J. C. Tilton. 2016. An active learning framework for hyperspectral image classification using hierarchical segmentation. *IEEE J. Sel. Topics Appl. Earth Observ. Remote Sens.* 9, 2 (2016), 640–654.
[51] X. L. Zhao, J. H. Yang, T. H. Ma, T. X. Jiang, M. K. Ng, and T. Z. Huang. 2022. Tensor completion via complementary global, local, and nonlocal priors. *IEEE Trans. Image Process.* 31 (2022), 984–999.
[52] Y.-B. Zheng, T.-Z. Huang, X.-L. Zhao, Q. Zhao, and T.-X. Jiang. 2021. Fully-connected tensor network decomposition and its application to higher-order tensor completion. In *Proc. AAAI Conf. Artif. Intell.*
[53] P. Zhou, C. Lu, J. Feng, Z. Lin, and S. Yan. 2021. Tensor low-rank representation for data recovery and clustering. *IEEE Trans. Pattern Anal. Mach. Intell.* 43, 5 (2021), 1718–1732.